

Gate-Defined Josephson Junctions in Magic-Angle Twisted Bilayer Graphene

Folkert K. de Vries,^{1,*} Elías Portolés,¹ Giulia Zheng,¹ Takashi Taniguchi,²
Kenji Wantanabe,³ Thomas Ihn,¹ Klaus Ensslin,¹ and Peter Rickhaus^{1,†}

¹*Solid State Physics Laboratory, ETH Zurich, CH-8093 Zurich, Switzerland*

²*International Center for Materials Nanoarchitectonics,*

National Institute for Materials Science, 1-1 Namiki, Tsukuba 305-0044, Japan

³*Research Center for Functional Materials, National Institute for Materials Science, 1-1 Namiki, Tsukuba 305-0044, Japan*

In the past two years, magic-angle twisted bilayer graphene^{1–4} has emerged as a uniquely versatile experimental platform that combines metallic, superconducting, magnetic and insulating phases in a single crystal^{5–10}. In particular the ability to tune the superconducting state with a gate voltage opened up intriguing prospects for novel device functionality. Here we present the first demonstration of a device based on the interplay between two distinct phases in adjustable regions of a single magic-angle twisted bilayer graphene crystal. We electrostatically define the superconducting and insulating regions of a Josephson junction and observe tunable DC and AC Josephson effects^{11,12}. We show that superconductivity is induced in different electronic bands and describe the junction behaviour in terms of these bands, taking in consideration interface effects as well. Shapiro steps, a hallmark of the AC Josephson effect and therefore the formation of a Josephson junction, are observed. This work is an initial step towards devices where separate gate-defined correlated states are connected in single-crystal nanostructures. We envision applications in superconducting electronics^{13,14} and quantum information technology^{15,16} as well as in studies exploring the nature of the superconducting state in magic-angle twisted bilayer graphene.

Gate-tunable superconductivity is a topical field of pure and applied physics research¹⁷, recently boosted by the realization of two-dimensional (2D) superconductors¹⁸. Switching superconductivity electrostatically on and off makes device design more flexible and circumvents interface and fabrication challenges met when working with multi-material nanostructures. Superconductivity in 2D has been realised for example at the LaAlO₃/SrTiO₃ interface¹⁹, and in van der Waals materials such as WTe₂^{20,21}. Because of the large charge carrier densities in most of these systems, in-situ electrostatic control is limited, and therefore gate-tunable Josephson junctions (JJs) have been realised only in a few systems^{19,22} where tunability is achieved by proximity to another material or by structural confinement.

Magic-angle twisted bilayer graphene (MATBG) is an ideal 2D platform for in-situ gate-tunable superconductivity^{5,7,9}. While there are numerous potential device applications^{13–16}, progress towards practical implementations has been hindered by the need for well-defined gated regions. Our multilayer gate technology has enabled us to create a device in a single MATBG crystal with electrostatically defined regions displaying distinct quantum phases. This device represents a new technology that can be used to build integrated 2D electronics using correlated states^{5–9}.

Here we report a first step towards superconducting devices based on distinct quantum phases within a single crystal, by engineering a tunable JJ electrostatically defined in MATBG (Fig. 1a,b). We confirm the formation of a JJ by observation of both the DC Josephson effect, with the typical hysteresis found for an underdamped JJ¹³, and the AC Josephson effect, see Figs. 1c,d. For the latter we apply a radio-frequency (rf) voltage excitation (V_{rf}), leading to the observation of Shapiro steps¹², that are proportional to the frequency f_{rf} and the superconducting flux quantum $h/2e$. Furthermore, we demonstrate that the device can be tuned in situ from the short to the long JJ regime, establishing the flexibility of our approach.

The device introduced here has three different gate layers that enable electrostatically defining several JJs (Fig. 1a,b). The global carrier density n in the MATBG can be changed by a graphite bottom gate. A pair of local top-gates (L, R) controls the density of the leads n_{ℓ} (when tuned together with the bottom gate) and defines a junction of length $L_j = 100$ nm and width $W = 2.3$ μm . The density in this junction n_j is gated by gate C. In order to form JJs with different lengths L_j we tune another gate or a combination of gates out of the superconducting state, which changes the regions of the device corresponding to densities n_{ℓ} and n_j accordingly. All measurements are performed at a temperature $T = 25$ mK (unless stated otherwise) in a two-terminal setup, where we apply a current I and measure the voltage V , from which the differential resistance R is calculated. We correct for contact and lead resistances in the I – V linetraces, but not in R colour maps. More details on the device fabrication and measurement setup are presented in Methods and Supplementary Information (SI), Sec. I.

Before returning to the JJ we introduce the energy bands and the bulk superconducting state in our MATBG device. In Fig. 2a we show R as a function of carrier density n . Peaks appear in R at the charge-neutrality point

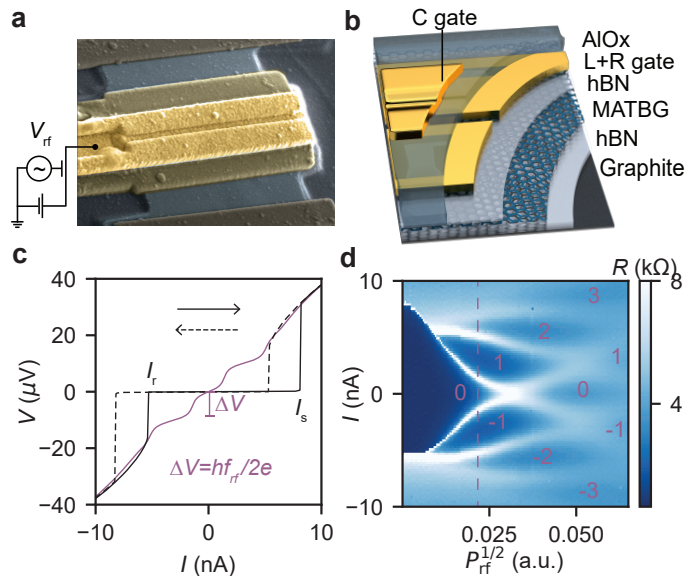


FIG. 1. DC and AC Josephson effect in a MATBG gate-defined Josephson junction. **a**, False-coloured, tilted scanning electron microscopy image of a similar device and **b**, cross-section diagram of the device. A 100 nm-long JJ is formed by tuning the MATBG into the superconducting state with the graphite bottom-gate and left (L) and right (R) top-gate electrodes, while the center (C) gate tunes the MATBG locally into a non-superconducting state. The gate electrodes are separated from the MATBG by insulating hexagonal boron nitride (hBN), and from each other by an aluminium-oxide (AIOx) layer. **c**, The applied current I and measured voltage V (black) reveal a switching and retrapping current (I_s and I_r) at density $n_j = -4.6 \times 10^{12} \text{ cm}^{-2}$ in the junction area. Applying a voltage drive (V_{rf}) at frequency $f_{rf}=5 \text{ GHz}$ to gate C induces Shapiro steps (violet). **d**, differential resistance R as a function of I and the square root of power ($P_{rf}^{1/2}$), showing the Shapiro step spectrum of the JJ. The step number is indicated, as is the trace plotted in **c**.

(CNP), and at full (n_s) and half-filling of the moiré bands, corresponding to a twist angle of $\theta = 1.06^\circ$. Based on this observation we sketch the energy bands and gaps¹⁻⁴ (inset Fig. 2a), containing the 1st moiré bands (blue and green), commonly referred to as the flat bands, with correlated insulator gaps at $n_s/2$ ^{6,9}. The 1st band is separated from the dispersive 2nd and 3rd moiré bands (violet) by a band gap. Note that the 2nd and 3rd band are separated in energy, which follows from measurements obtained in the JJ-device configuration (Fig 3a,b), but contradicts existing band-structure calculations¹⁻⁴. To reveal the superconducting behaviour of the device we measure the differential resistance R as a function of current I and density n (Fig. 2b). We observe plateaus and the typical peak in R at critical supercurrent I_c , where the device switches out of the bulk superconducting state. The largest I_c is observed at $n = -1.5 \times 10^{12} \text{ cm}^{-2}$ in the superconducting dome around $-n_s/2$. Around $+n_s/2$ a smaller superconducting dome is observed. This in accordance with earlier reported phase diagrams for MATBG of $\theta = 1.06^\circ$ ^{5,7}. We estimate a superconducting coherence length $\xi = 70 \text{ nm}$ from I_c measurements as a function of temperature T and perpendicular magnetic field B_\perp (SI Sec. II).

Having established superconductivity in the MATBG device, we describe the effect of detuning n_j while keeping n_ℓ superconducting. Figure 3a,b shows R at fixed I (top panels) as well as its dependence on I (bottom panels) as a function of n_j , while n_ℓ is close to $-n_s/2$ (a) or to $+n_s/2$ (b), respectively. As the quasiparticle current and the capacitance between the contacts influences the maximum supercurrent¹³, we refer to this as the ‘switching current’ I_s from now on. Comparing the measurements to the bulk behaviour shown in Fig. 2b, we still observe a finite I_s when n_j is tuned out of the superconducting state. That is, we observe the DC Josephson effect. Note that when $n_j=n_\ell$ the entire device is superconducting (shaded regions in Figs. 3c,d). In Fig. 3a,b the JJ length $L_j = 100 \text{ nm}$ is on the order of the estimated $\xi = 70 \text{ nm}$, indicative of the short JJ regime^{13,23}. Also, for the JJ with $n_\ell = -1.5 \times 10^{12} \text{ cm}^{-2}$ we observe signatures of ballistic transport²⁴ (SI Sec. III); I_s is thus expected to be limited by the interfaces. In addition to the JJs with $L_j = 100 \text{ nm}$, our device allows us to realize other lengths, by using combinations of gates L (650 nm), R (650 nm) and C (100 nm). Overall, I_s as a function of n_j is reduced for increased L_j , as presented in Fig. 3c,d, and in the inset of Fig. 3c, consistent with $L_j \gg \xi$ for the $L_j = 650 \text{ nm}$ and 1400 nm JJs, which means that these junctions are in the long-JJ regime^{13,23} where the transport in the junction area is limiting I_s .

By changing n_j we tune the JJs through the energy bands depicted in Fig. 2a, as reflected in the R trace in Fig. 3a,b (highlighted with corresponding background colours). We now analyse how I_s changes with n_j , discuss this in terms

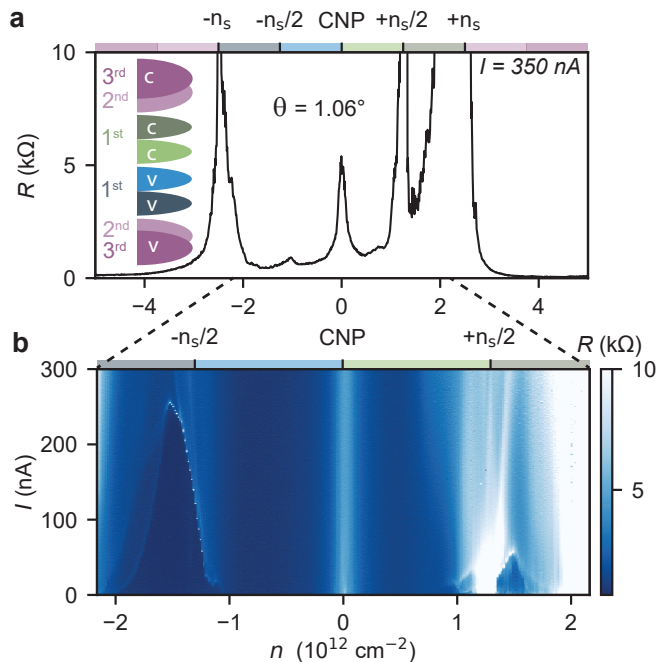


FIG. 2. **Bulk superconductivity in MATBG.** **a** R as a function of n shows pronounced peaks for $\pm n_s$ and $\pm n_s/2$, symmetrically around the CNP. The inset shows a schematic representation of the energy bands in MATBG, where the flat valence (v) and conduction (c) bands (blue and green) and higher moiré bands (violet) are indicated. The colours on top of the panels indicate the relation between the density and the bands. **b** R as a function of I and n reveals superconductivity around $\pm n_s/2$.

of the junction area (N area) and the interfaces between the leads and the junction (N–S interfaces). We observe step-like reductions in I_s when n_j crosses over to another band and a more gradual change of I_s within a given band (Fig. 3a,b). These steps in I_s occur when the Fermi level crosses a band gap at the CNP and at $n_j = \pm n_s$, and a correlated insulator gap at $n = \pm n_s/2$, which reduces the transparency of the N–S interfaces. We note that the abrupt changes can also have a contribution from differences between the eigenstates on each side of the interface, such as topological indices¹⁰ or valley/spin flavours²⁵. Schottky barriers and interfacial defects can be neglected as the S–N interfaces are created in a single crystal. Regarding the gradual change of I_s within a band, we suspect the Fermi velocity v_F to be most important for the proximity effect. BCS theory predicts ξ in the junction area to scale linearly with v_F of the carriers in the N area¹³. Also, the N–S interface transparency is affected by a mismatch between v_F in the leads and in the N area²⁶, respectively. The dramatic changes in v_F with n in the bands of MATBG^{1–4} therefore impacts the induced superconductivity. Note that L_j slightly changes due to the gate geometry used. For increasing $|n_j - n_\ell|$, L_j could increase by approximately 20 nm (SI Sec. I).

In the 1st moiré bands (blue and green) we observe rather large I_s values, in line with the weakly insulating states at $\pm n_s/2$ and the CNP, leading to a significant I_s even if the junction is 1400 nm long (Fig. 3c). For $L_j = 650$ nm we observe a non-monotonic behaviour of I_s between $-n_s/2$ and the CNP (red arrow in Fig. 3c). This could be due to an optimum in v_F , or might be caused by electron correlations that are already present, yet not strong enough to cause a superconducting ground state in our device⁹.

An interesting JJ is realized once n_j is tuned to the opposite superconducting dome. The switching current I_s is increased around $-n_s/2$ for all three L_j values as shown in Fig. 3b,d, as well as for $L_j = 650$ nm and 1400 nm as shown in Fig. 3c. If the leads and junction in this S–S–S configuration exhibit the same superconducting state, I_s would solely depend on the interfaces and not on L_j . We observe, however, a dependence on L_j in both Fig. 3c and d, suggesting that the superconductivity in the two domes differ. Such a scenario is an interesting avenue for future research, as it could be possible that we formed a JJ with two distinct superconductors.

When we tune n_j into the 2nd and 3rd moiré band (violet colours in Fig. 2a), I_s in Fig. 3(a,b) is greatly reduced, due to a crossing of the gap ($\pm n_s$) at the N–S interfaces. In addition, another step in R is observed for both the valence bands in Fig. 3a, as well as for the conduction bands in Fig. 3b. At the same time, I_s is either reduced to zero, respectively. Based on this observation and supported by Fabry-Pérot oscillations (SI Sec. III), we infer that we observe the band edge of the 3rd moiré band, and this band is therefore offset in energy with respect to the 2nd

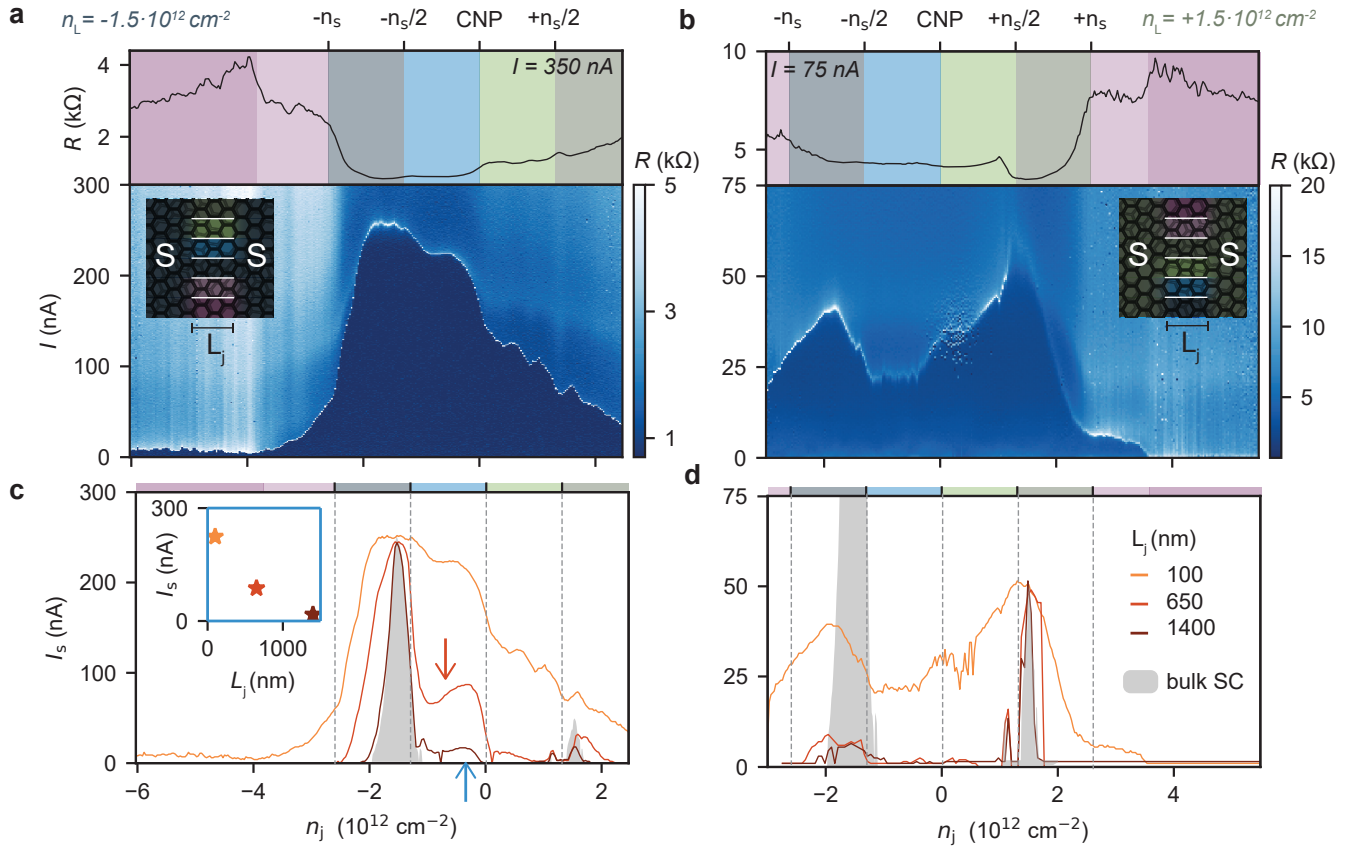


FIG. 3. **Gate-defined and tunable Josephson junctions.** **a,b**, Gate-defined JJs with $L_j = 100$ nm and n_ℓ tuned to either the negatively (a) or positively doped (b) superconducting domes as indicated on the top axis. The line trace, taken at the I value indicated, and colour-map plot R as a function of n_j (and I). Overlaid are the colours indicating of energy bands sketched in Fig. 1a. **c,d**, I_s for different L_j as a function of n_j . Bulk I_c versus n is plotted for reference (grey). The inset displays I_s versus L_j for n_j indicated by the blue arrow.

moiré band (Fig. 2a). While before we connected the abrupt changes of R and I_s to the Fermi level crossing a gap, this is unlikely to be the case here, as we do not observe a resistance peak in Fig. 2a around $n = -4.6 \times 10^{12} \text{ cm}^{-2}$. We speculate that the transition could occur because of a sudden change in v_F (mismatch) or a mismatch in eigenstates in the leads and the junction.

We further studied this n_j -regime for the 100 nm JJ with $n_\ell = -1.5 \times 10^{12} \text{ cm}^{-2}$ by measuring the AC Josephson effect. As n_j is tuned into the 2nd and 3rd moiré band, where the N–S interfaces are less transparent, we observe the AC Josephson effect in the form of Shapiro steps¹². In the 3rd moiré band ($n_j = -4.6 \times 10^{12} \text{ cm}^{-2}$) the steps have the trivial height of $\Delta V = (h/2e) \times f_{\text{rf}}$ for both frequencies of $f_{\text{rf}} = 5$ GHz and 1.81 GHz, see Fig. 1c,d, and Fig. 4a, respectively, and SI Sec. IV. Also, no integer steps are missing or only occurring at a specific $P_{\text{rf}}^{1/2}$, as could be expected for a topological JJ²⁷. Therefore, our data suggests that the superconductivity around $n_s/2$ is of trivial rather than of topological nature.

The Shapiro-step spectrum for n_j tuned in the 2nd moiré band only ($n_j = -3.5 \times 10^{12} \text{ cm}^{-2}$) in Fig. 4b shows a dependence on $P_{\text{rf}}^{1/2}$ very different from that in Fig. 4a. The steps are less dense and fade more quickly with respect to $P_{\text{rf}}^{1/2}$. We attribute the fading to thermal and impurity smearing of R , impacting the lower-valued R -peaks in Fig. 4b more than in Fig. 4a. In addition, the hysteresis (I_s/I_T) differs, suggesting a change in the JJ that can be traced back to the onset of the 3rd moiré band as the n_j -dependence in Fig. 4e reveals.

We compare the trend of this JJ behaviour to simulations using the resistively and capacitively shunted junction model¹³ (see Methods for details). In this model, the resistance R_j , allowing for the flow of normal current, and C_j , the capacitance between the leads, are both connected in parallel to an ideal JJ with a given I_c . Together, these parameters are captured in the Stewart–McCumber parameter $\beta \propto I_c R_j^2 C_j$. In the inset of Fig. 4b, we show the simulated I_s/I_T as a function of β , and we estimate $\beta = 4.2$ and $\beta = 1.5$ for the I_s/I_T from Fig. 4a,b, respectively.

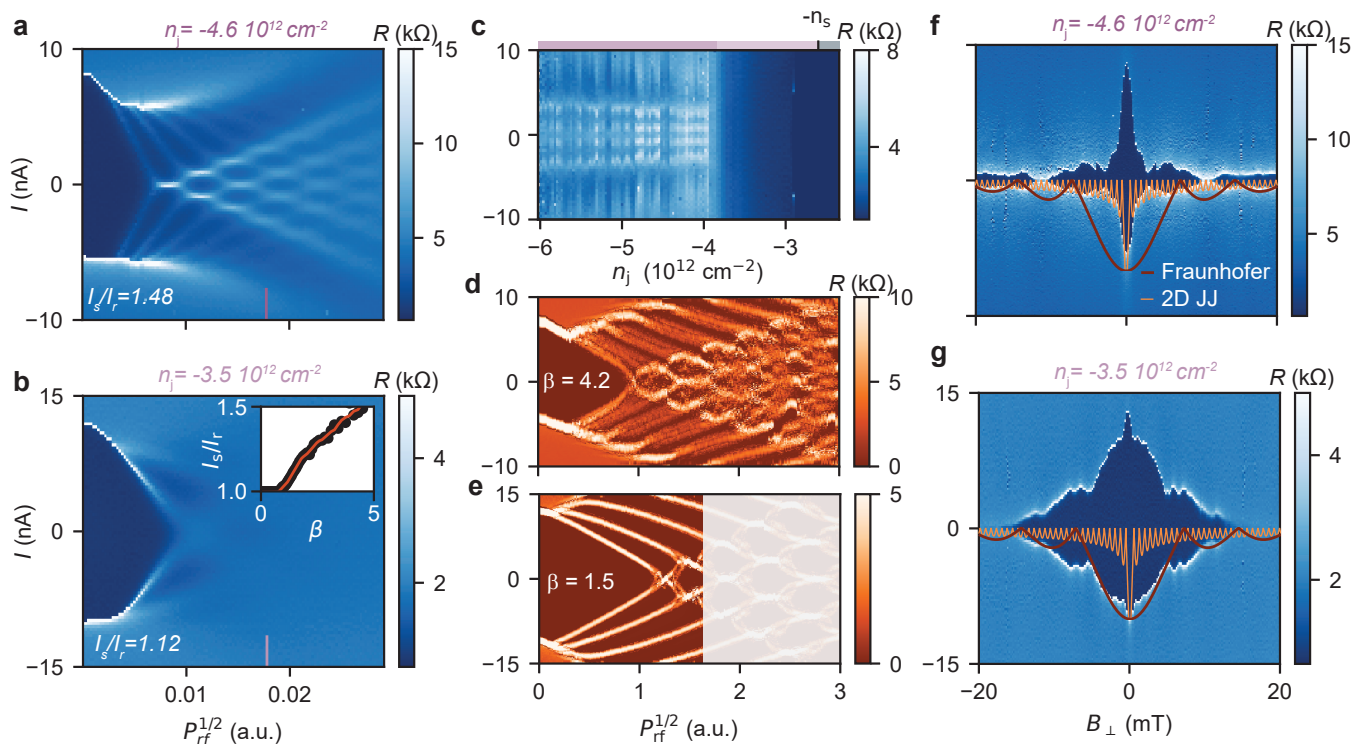


FIG. 4. **AC Josephson effects for the 2nd and 3rd moiré band.** **a,b**, Measurement of the Shapiro steps, visible in R versus I for different $P_{\text{rf}}^{1/2}$, for n_j as indicated. The hysteresis I_s/I_r is given. The inset in **b** shows the calculated I_s/I_r for different β . **c**, R versus I measured as a function of n_j at $P_{\text{rf}}^{1/2}$ indicated in **c,d**. The colour bar on top refers to the bands in Fig. 2a. **d,e**, Shapiro steps simulated using the resistively and capacitively shunted junction (RCSJ) model (see Methods) using the β value indicated, $R_j = 2.5 \text{ k}\Omega$ and $R_j = 1.14 \text{ k}\Omega$ for the upper and lower panels, respectively, and $C_j = 32 \text{ fF}$ for both. The shaded area in **e** is added for better comparability. **f,g**, R as a function of I and B_{\perp} shows the magnetic interference pattern of the 100 nm JJ with $n_{\ell} = -1.5 \times 10^{12} \text{ cm}^{-2}$ for the n_j value indicated. For both scenarios we plotted a theoretical model for a 3D JJ and for a JJ in a 2D superconductor.

Then, we simulate Shapiro-step spectra using β , the measured I_s , a constant C_j (the device geometry is constant), and we choose $R_j = 2.5 \text{ k}\Omega$ based on the normal-state resistance for $\beta = 4.2$, of which $R_j = 1.14 \text{ k}\Omega$ for $\beta = 1.5$ follows from the earlier-mentioned constraint on C_j . The simulated spectra in Fig. 4d qualitatively reproduce the measured spectra of Fig. 4a,b. As the smearing is not captured in the model, we added a semi-transparent box in Fig. 4e for better comparability. The increase of R_j when entering the 3rd moiré band means that the quasiparticle transport through the junction is reduced, which can be important for future device applications such as detectors^{13,14}.

Lastly, we report magnetic interference measurements in this n_j -regime and compare them to theoretical models (see Methods). In a textbook 3D JJ, applying B_{\perp} results in a modulation of I_s described by a Fraunhofer pattern with the periodicity $\Delta B_{\perp} = h/2e/(L_j W)$, and I_s -maxima that scale with $1/B_{\perp}$ ¹³. For a JJ in a 2D superconductor, B_{\perp} also penetrates the leads, and $\Delta B_{\perp} = 1.8\Phi_0/W^2$ and the I_s -maxima scale with $1/B_{\perp}^{1/2}$ ²⁸. In Fig. 4f at $n_j = -4.6 \times 10^{12} \text{ cm}^{-2}$, the I_s -maxima follow the $1/B_{\perp}^{1/2}$ behaviour, but the periodicity matches neither theoretical pattern. The ill-defined periodicity is likely to be caused by disorder in the junction area and the leads due to twist-angle inhomogeneity²⁹. For the interference pattern shown in Fig. 4g, measured at $n_j = -3.48 \times 10^{12} \text{ cm}^{-2}$, I_s is closer to the $1/B_{\perp}$ scaling of a Fraunhofer pattern. However, it also lacks a clear periodicity, even though the smaller I_s oscillations on the larger background compare better to the 2D JJ pattern. Although we find clearly different interference patterns, further theoretical and experimental work is needed to understand the patterns themselves.

In conclusion, we have shown a proof-of-principle gate-defined superconducting device in MATBG, and explored this JJ by tuning through the different moiré bands. We defined JJs with different lengths and different superconducting states in a single device, establishing the flexibility of our approach. This work enables future technological applications, by virtue of its planar and gate-tunable superconductivity^{15,16}, as well as future investigations of the nature of the superconducting state in MATBG, for example by fabricating superconducting quantum interference devices or by creating JJs with a ferromagnetic barrier.

METHODS

Device Fabrication

We assemble the heterostructure using the dry pick-up method³⁰. As a first step, a large ($> 40 \mu\text{m} \times 40 \mu\text{m}$) mechanically exfoliated graphene flake is identified on a p:Si/SiO₂ (285 nm) wafer. The graphene flake is scratched into two pieces using a sharp (2.5 μm tip diameter) tungsten needle which is controlled by a micromanipulator. Using a PDMS/PC stamp, the top hBN layer (27 nm) is picked up at a $T = 80^\circ\text{C}$. At 40°C , we pick up the first graphene piece, rotate the stage by 1.1° and pick up the second piece. The twisted graphene is encapsulated with a bottom hBN flake (24 nm), the flake is in contact with the stack at 40°C and picked up at 80°C . At the same temperature, the graphite layer is picked up. PC is detached from PDMS at 150°C and removed in dichloromethane. The top and bottom hBN thicknesses are determined using atomic force microscopy (AFM). AFM images serve to identify clean and bubble-free regions of the stack. Next, we define 1D contacts³¹ to graphene by electron beam lithography (EBL), reactive ion etching (RIE, CHF₃/O₂, 40/4sccm, 60 W, with a 0.6 nm/s hBN etching rate, for 68 s) and electron beam evaporation (Cr/Au, 10/70 nm). Then, top-gates are defined by EBL (Cr/Au, 10/60 nm) and the graphene is etched (RIE, CHF₃/O₂, 40/4sccm, 60 W, 120 s, followed by O₂, 40sccm, 60 W, 10 s). Using atomic layer deposition (ALD), 30 nm of AlO_x are deposited at $T = 150^\circ\text{C}$. In a final step, we define the central gates by EBL and deposit Cr/Au, 10/110 nm.

Measurement setup

We use a DC voltage source built in-house with a $10 \text{ M}\Omega$ connected in series to generate the bias current, amplify the voltage using a voltage amplifier built in-house and measure it with an Hewlett Packard 34401A multimeter. We measure in a 2 terminal setup, and subtracted a series resistance of 785Ω in Fig. 1b. The bottom gate, L gate and R gate are each connected to a DC voltage source. The C gate is connected to a DC voltage source and, using a bias T with $R = 10 \text{ k}\Omega$ and $C = 10 \text{ nF}$, to a Rohde und Schwarz SMB 100A signal generator.

RCSJ model

We model our JJ with the resistively and capacitively shunted junction (RCSJ) model¹³. Replacing the voltage across the junction, V , with the superconducting phase between the two electrodes of the junction, ϕ , using $V = (\Phi_0/2\pi) \times d\phi/dt$ ¹¹, we obtain the second order differential equation with reduced units³².

$$\frac{I}{I_c} = \sin \phi + \frac{d\phi}{d\tilde{\tau}} + \beta \frac{d^2\phi}{d^2\tilde{\tau}^2}, \quad (1)$$

containing the Stewart–McCumber parameter

$$\beta = \frac{2\pi R_j^2 C_j I_c}{\Phi_0}, \quad (2)$$

and $\tilde{\tau} = t/\tau_J$ with

$$\tau_J = \frac{\Phi_0}{2\pi R_j I_c} \quad (3)$$

being the Josephson time constant.

The resistance R_j depends on the state of the junction. When operating it beyond its critical current, R_j corresponds to R_n , the normal state resistance of the junction. When a supercurrent is flowing, R_j accounts for tunnelling of quasiparticles through the junction. The quasiparticle resistance R_{qp} is, in general, expected to be higher than R_n . It is hard to estimate the value of R_{qp} and its dependence on the current I , especially since our knowledge about the electronic state in the junction area is limited. We have therefore decided to assume R_j is on the order of R_n .

The switching current to retrapping current ratio I_s/I_r is directly related to β^{13} . Since there exists no exact analytical relation between the parameters, we compute it (inset in Fig. 4b). We then obtain $\beta_C = 4.2$ and $\beta_C = 1.5$ for $n_j = -4.6 \times 10^{12} \text{cm}^{-2}$ and $n_j = -3.5 \times 10^{12} \text{cm}^{-2}$ respectively.

For modelling the behavior of an RF-driven Josephson junction we add a sinusoidal term to the current bias term of equation (1), thus obtaining

$$\frac{I}{I_c} + \frac{I_{\text{RF}}}{I_c} \sin \tilde{\omega} \tilde{\tau} = \sin \phi + \frac{d\phi}{d\tilde{\tau}} + \beta_C \frac{d^2\phi}{d\tilde{\tau}^2} \quad (4)$$

with $\tilde{\omega} = \omega_{\text{RF}} \tau_J$ the reduced angular frequency of the RF-source³³.

In this mathematical treatment we neglect the frequency-dependent coupling of the RF-signal to the junction. Furthermore, we assume the relationship between the sinusoidal voltage of the RF-wave and the resulting AC current through the junction to be linear.

The reduced angular frequency, $\tilde{\omega}$, is the relevant parameter for the observation of the Shapiro steps. Only if the condition $\tilde{\omega} \ll 1$ is fulfilled, the phase of the junction is properly locked to that of the RF-source, and Shapiro steps can be observed³⁴. Three parameters determine $\tilde{\omega}$: The RF-frequency, which is in our simulations always fixed to $\omega_{\text{RF}} = 1.81 \text{GHz}$, the critical current of the junction, which we fix to either $I_C = 7 \text{nA}$ or $I_C = 12 \text{nA}$, and the resistance R of the junction. As we mentioned previously, we extract experimentally $\beta_C \propto I_C C R^2$, which leaves us with two free parameters for our modelling, R and C . We start at $\beta_C = 4.2$ and choose $R = 2.5 \text{k}\Omega$ since it is of the order of the normal state resistance for $n_j = -4.6 \times 10^{12} \text{cm}^{-2}$. We compute the resulting capacitance $C = 31.2 \text{fF}$ and perform the simulation (4d). When moving to $\beta_C = 1.5$, for simulating the $n_j = -3.5 \times 10^{12} \text{cm}^{-2}$ case, we keep C constant and obtain $R = 1.14 \text{k}\Omega$, obtaining the result shown in Fig. 4e.

Magnetic interference patterns

Here we provide the equations used to plot the theoretical magnetic interference patterns. The Fraunhofer interference pattern follows

$$I(B_{\perp}) = I_c \left| \frac{\sin(\pi B_{\perp} L_j W / \Phi_0)}{\pi B_{\perp} L_j W / \Phi_0} \right|. \quad (5)$$

For the Josephson junction in a 2D superconductor we use the approximation

$$I(B_{\perp}) = 0.61 \frac{I_c}{W} \sqrt{\frac{\Phi_0}{|B_{\perp}|}} |\cos(1.72 |B_{\perp}| W^2 / \Phi_0 - \pi/4)|. \quad (6)$$

given in Ref. 28.

* devriesf@phys.ethz.ch

† peterri@phys.ethz.ch

-
- [1] Suárez Morell, E., Correa, J. D., Vargas, P., Pacheco, M. & Barticevic, Z. Flat bands in slightly twisted bilayer graphene: Tight-binding calculations. *Phys. Rev. B* **82**, 121407 (2010).
- [2] Bistritzer, R. & MacDonald, A. Moiré bands in twisted double-layer graphene. *Proc. Natl. Acad. Sci.* **108**, 12233 – 12237 (2011).
- [3] Nam, N. N. T. & Koshino, M. Lattice relaxation and energy band modulation in twisted bilayer graphene. *Phys. Rev. B* **96**, 075311 (2017).
- [4] Guinea, F. & Walet, N. R. Continuum models for twisted bilayer graphene: Effect of lattice deformation and hopping parameters. *Phys. Rev. B* **99**, 205134 (2019).
- [5] Cao, Y. *et al.* Unconventional superconductivity in magic-angle graphene superlattices. *Nature* **556**, 43–50 (2018).
- [6] Cao, Y. *et al.* Correlated insulator behaviour at half-filling in magic-angle graphene superlattices. *Nature* **556**, 80–84 (2018).
- [7] Yankowitz, M. *et al.* Tuning superconductivity in twisted bilayer graphene. *Science* **363**, 1059–1064 (2019).
- [8] Sharpe, A. L. *et al.* Emergent ferromagnetism near three-quarters filling in twisted bilayer graphene. *Science* **365**, 605–608 (2019).
- [9] Lu, X. *et al.* Superconductors, orbital magnets and correlated states in magic-angle bilayer graphene. *Nature* **574**, 653–657 (2019).
- [10] Nuckolls, K. P. *et al.* Strongly correlated chern insulators in magic-angle twisted bilayer graphene. *arXiv preprint arXiv:2007.03810* (2020).
- [11] Josephson, B. Possible new effect in superconducting tunneling. *Phys. Lett.* **1**, 251–253 (1962).
- [12] Shapiro, S. Josephson currents in superconducting tunneling: The effect of microwaves and other observations. *Phys. Rev. Lett.* **11**, 80–82 (1963).
- [13] Tinkham, M. *Introduction to superconductivity* (Courier Corporation, 2004).
- [14] Braginski, A. I. Superconductor electronics: Status and outlook. *J. Supercond. Nov. Magn.* **32**, 23–44 (2019).
- [15] Wendin, G. Quantum information processing with superconducting circuits: a review. *Rep. Progr. Phys.* **80**, 106001 (2017).
- [16] Liu, X. & Hersam, M. C. 2d materials for quantum information science. *Nat. Rev. Mater.* **4**, 669–684 (2019).
- [17] De Simoni, G., Paolucci, F., Solinas, P., Strambini, E. & Giazotto, F. Metallic supercurrent field-effect transistor. *Nat. Nanotechnol.* **13**, 802–805 (2018).
- [18] Saito, Y., Nojima, T. & Iwasa, Y. Highly crystalline 2d superconductors. *Nat. Rev. Mater.* **2**, 16094 (2016).
- [19] Caviglia, A. D. *et al.* Electric field control of the laalo3/srtio3 interface ground state. *Nature* **456**, 624–627 (2008).
- [20] Fatemi, V. *et al.* Electrically tunable low-density superconductivity in a monolayer topological insulator. *Science* **362**, 926–929 (2018).
- [21] Sajadi, E. *et al.* Gate-induced superconductivity in a monolayer topological insulator. *Science* **362**, 922–925 (2018).
- [22] Kononov, A. *et al.* One-dimensional edge transport in few-layer wte2. *Nano Lett.* **20**, 4228–4233 (2020).
- [23] Li, C., Guéron, S., Chepelianskii, A. & Bouchiat, H. Full range of proximity effect probed with superconductor/graphene/superconductor junctions. *Phys. Rev. B* **94**, 115405 (2016).
- [24] Calado, V. E. *et al.* Ballistic josephson junctions in edge-contacted graphene. *Nat. Nanotechnol.* **10**, 761–764 (2015).
- [25] Xie, M. & MacDonald, A. H. Weak-field hall resistivity and spin/valley flavor symmetry breaking in matbg. *arXiv preprint arXiv:2010.07928* (2020).
- [26] Mortensen, N. A., Flensberg, K. & Jauho, A.-P. Angle dependence of andreev scattering at semiconductor–superconductor interfaces. *Phys. Rev. B* **59**, 10176–10182 (1999).
- [27] Bocquillon, E. *et al.* Gapless andreev bound states in the quantum spin hall insulator hgte. *Nat. Nanotechnol.* **12**, 137–143 (2017).
- [28] Moshe, M., Kogan, V. G. & Mints, R. G. Edge-type josephson junctions in narrow thin-film strips. *Phys. Rev. B* **78**, 020510 (2008).
- [29] Uri, A. *et al.* Mapping the twist-angle disorder and landau levels in magic-angle graphene. *Nature* **581**, 47–52 (2020).
- [30] Kim, K. *et al.* van der Waals Heterostructures with High Accuracy Rotational Alignment. *Nano Lett.* **16**, 1989–1995 (2016).
- [31] Wang, L. *et al.* One-dimensional electrical contact to a two-dimensional material. *Science* **342**, 614–617 (2013).
- [32] Orlando, T. P. & Delin, K. A. *Foundations of Applied Superconductivity* (Addison Wesley, 1991).
- [33] Russer, P. Influence of microwave radiation on current-voltage characteristic of superconducting weak links. *J. Appl. Phys.* **43**, 2008–2010 (1972).
- [34] Le Calvez, K. *et al.* Joule overheating poisons the fractional ac josephson effect in topological josephson junctions. *Commun. Phys.* **2**, 4 (2019).

ACKNOWLEDGEMENTS

We thank Benedikt Kratochwil, Peter Maerki and the staff of the ETH cleanroom facility FIRST for technical support, and Tobias Wolf for useful discussions. We acknowledge support from the Graphene Flagship and from the European Union's Horizon 2020 research and innovation programme under grant agreement No 862660/QUANTUM E LEAPS. K.W. and T.T. acknowledge support from the Elemental Strategy Initiative conducted by the MEXT, Japan, Grant Number JPMXP0112101001, JSPS KAKENHI Grant Number JP20H00354 and the CREST(JPMJCR15F3), JST. E.P. acknowledges support from La Caixa Foundation.

AUTHOR INFORMATION

Corresponding authors

Correspondence and requests for materials should be addressed to Folkert K. de Vries (devriesf@phys.ethz.ch) and Peter Rickhaus (peterri@phys.ethz.ch).

Author contributions

E.P. made the stack and P.R. fabricated the device, with assistance from G.Z. T.T. and K.W. supplied the hBN crystals. F.K.d.V. and E.P. performed the measurements. E.P. performed the simulations. T.I., K.E. and P.R. supervised the project. F.K.d.V., P.R. and E.P. wrote the manuscript with comments from all authors.

Competing interests

The authors declare no competing financial interests.

Supplementary Information

I. DEVICE

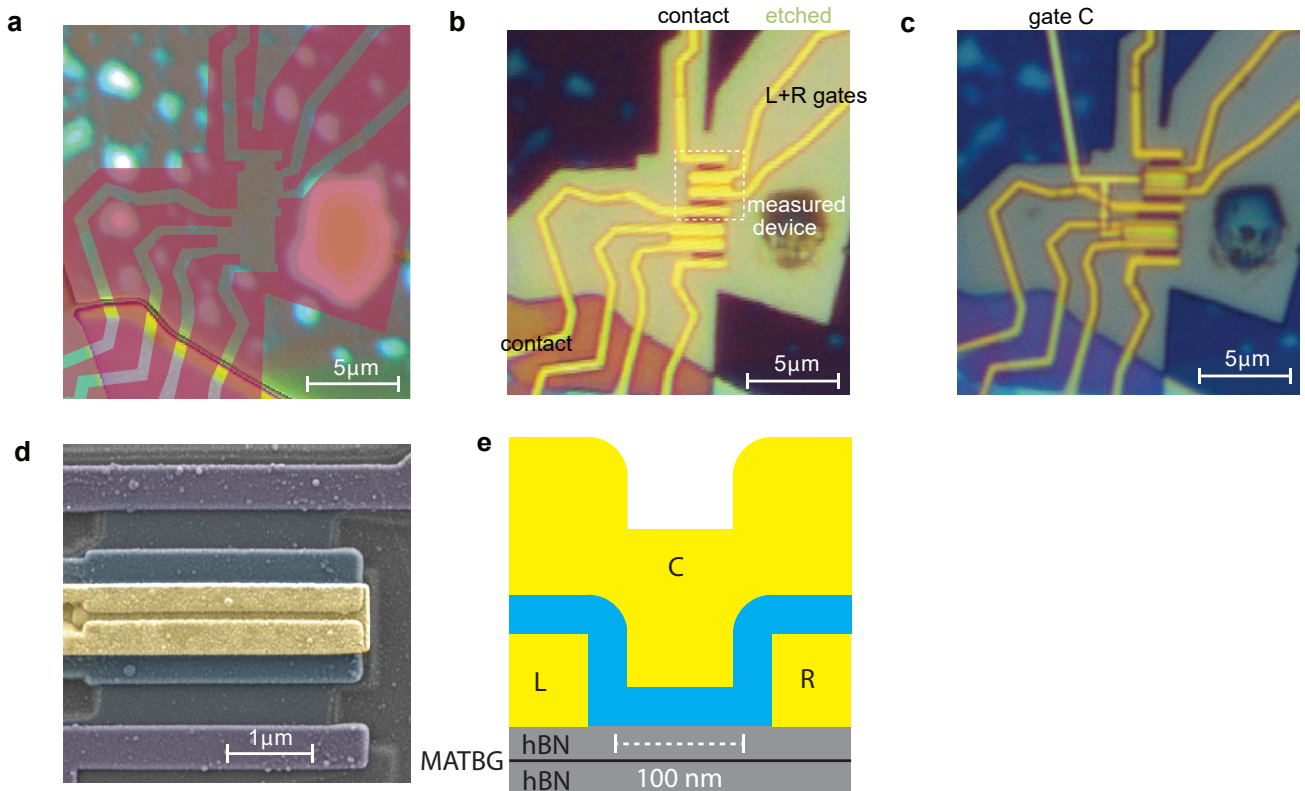


FIG. S1. **Fabrication images of the device.** **a** Optical image before fabrication, the red shaded area is the etch mask. **b** Optical image before and **c** after deposition of the central gate electrodes. **d** Scanning electron microscopy image of a similar device (not titled). **e** Schematic cross-section of the device, all layers are to scale.

In Fig. S1a-c we show optical images of the device fabrication process. The measured device is marked with a dashed square. Figure S1a shows that the device is placed carefully in-between the bubbles in the MATBG. The bubbles are expected to lead to twist angle inhomogeneity²⁹. In transport, we find that the lower device has a larger twist angle ($\theta = 1.5^\circ$) and does not show superconductivity. The narrow gap between the L+R gates is well resolved in the SEM image in Fig. S1c, allowing us to identify a typical length of 100 nm. The SEM image is taken from a similar device fabricated in the same batch and with similar geometry as the measured device (i.e. same length of L+R gates and same gap between these gates in the design file). The schematic cross-section in Fig. S1e shows this length. Also, we estimate that the size of the gated region below gate C can vary by ± 10 nm.

II. CRITICAL CURRENT DEPENDENCE ON TEMPERATURE AND MAGNETIC FIELD

We measure I_c as a function of temperature T and perpendicular magnetic field B_\perp at $n = -1.53 \times 10^{12} \text{ cm}^{-2}$, and present the result in in Fig. S2. The extracted critical magnetic field allows us to fit the Ginzburg–Landau equation $B_{\perp,c} = (\hbar/2e)/\xi^2(1 - T/T_c)$ for two-dimensional superconductors¹³, and obtain an estimate of the superconducting coherence length ξ .

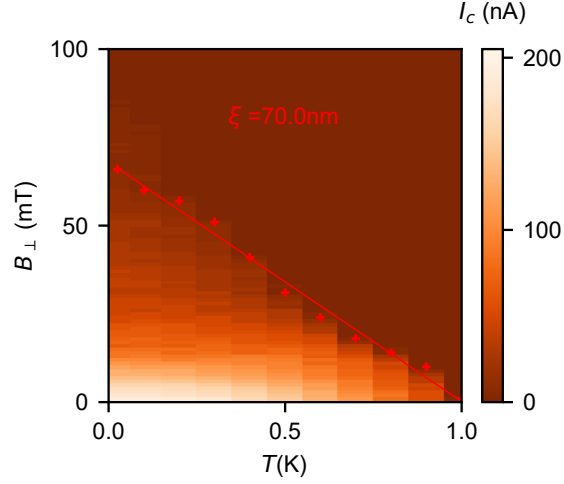


FIG. S2. I_c versus B_\perp and T . The critical magnetic field is extracted and plotted as red crosses. A fit with the Ginzburg–Landau theory provides us with the estimate of the superconducting coherence length ξ indicated.

III. FABRY-PÉROT OSCILLATIONS

In addition to the step in R observed in the dispersive bands, we investigate Fabry-Pérot resonances for the 100 nm JJ with $n_\ell = -1.5 \times 10^{12} \text{ cm}^{-2}$, similar to earlier work in proximitized graphene JJs²⁴. In Fig. S3a,b we show a zoom-in to the region where I_s is modulated by $\sqrt{n_j}$ for $n_j < n_s$. The conductance G in Fig. S3c, recorded at $I = 350 \text{ nA}$, behaves in a similar fashion. Local maximum values of I_c and G occur if the Fabry-Pérot condition is fulfilled. For constructive interference the condition reads $i\lambda = 2l$, where i is an integer, λ the charge carrier wavelength and l the cavity length. The condition can be expressed as a function of density by using $\lambda = 2\pi/k$ and $k = \sqrt{(4/g)n_i\pi}$, giving $n_i = \pm\pi i^2/l^2(4/g)$. The third valence band is expected to be 4-fold degenerate thus $g = 4$. The observed maxima in I_c and G (Fig. S3b,c) are well captured by setting $l = 75 \text{ nm}$ (indicated by orange dotted lines) which is in good agreement with L_j .

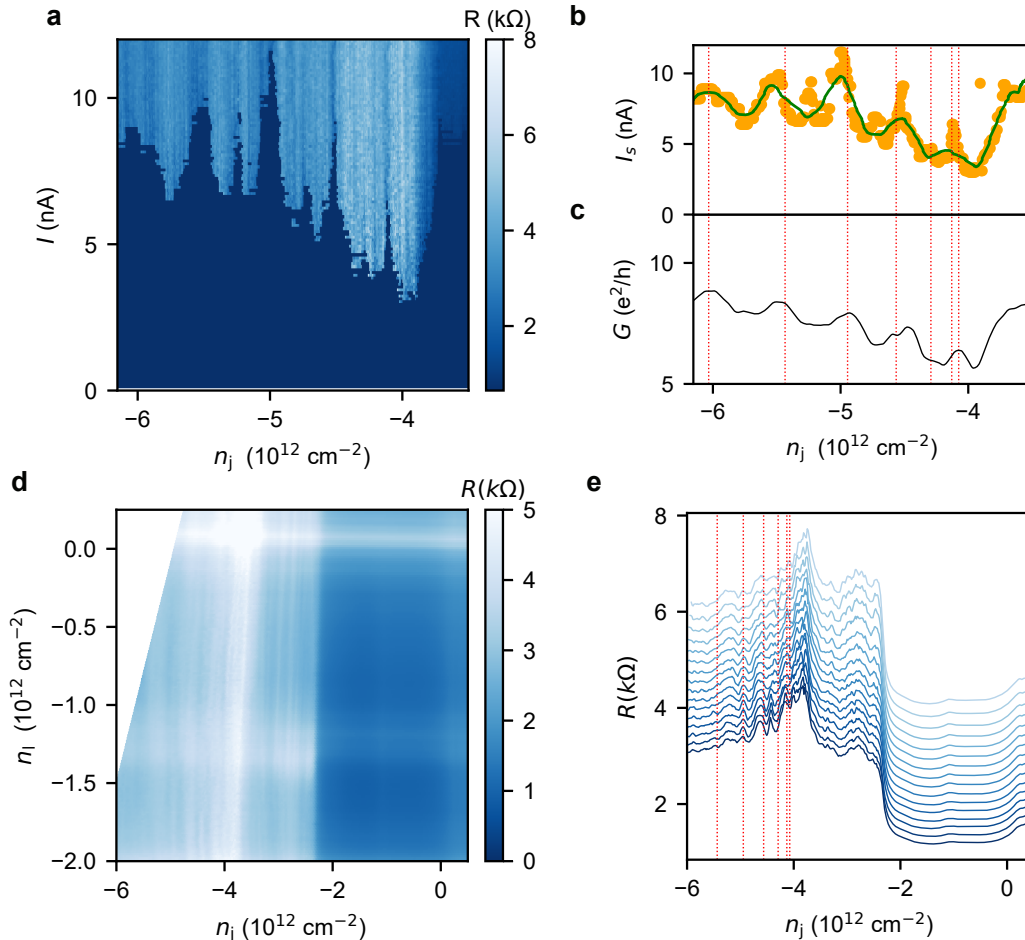


FIG. S3. **Fabry-Pérot oscillations at the onset of the 3rd moiré band.** **a** Zoom in on R versus I and n_j for the JJ of 100 nm and $n_\ell = -1.5 \times 10^{12} \text{ cm}^{-2}$. **b** I_s versus n_j extracted from **a** and a smoothed curve fit through it. **c** G versus n_j calculated at $I = 350 \text{ nA}$. **d** R as a function of n_ℓ and n_j , at $I = 350 \text{ nA}$. **e** Extracted line-traces from (a). The orange dotted lines mark conditions for destructive Fabry-Pérot interference, assuming a cavity length of 75 nm.

We further confirm the ballistic origin of the oscillations by investigating the dependence on n_ℓ , see Fig. S3d,e, where we plot $R(n_j, n_\ell)$. The Fabry-Pérot oscillations show little dependence on n_ℓ , confirming that the oscillations originate from a region below gate C. Such behavior becomes clear in the line traces $R(n_j)$ for different n_ℓ , see Fig. S3e, where the n_j at which we expect constructive Fabry-Pérot oscillations are indicated by orange dotted lines.

IV. SHAPIRO STEP LINE TRACES

In Fig. S4a,b we show line traces of the Shapiro-step spectra at both frequencies 5.1 GHz and 1.8 GHz. We observe that the steps occur at the expected voltage following $\Delta V = hf_{\text{rf}}/2e$.

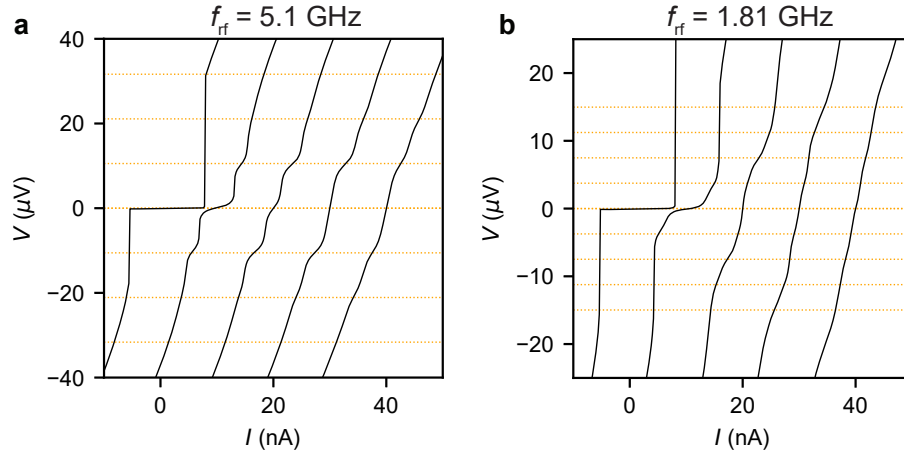


FIG. S4. **Line traces of Shapiro steps at different frequencies.** **a,b** V versus I show shapiro step line traces for the JJ of 100 nm with $n_j = -4.6 \times 10^{12} \text{ cm}^{-2}$ $n_\ell = -1.5 \times 10^{12} \text{ cm}^{-2}$ for the frequencies indicated. The traces are offset by 10 nA and taken at $P_{\text{rf}}^{1/2} = 0, 0.015, 0.022, 0.028, 0.035$ for **a**, and $P_{\text{rf}}^{1/2} = 0, 0.005, 0.009, 0.014, 0.019$. The orange dashed lines mark the expected steps at multiples of $\Delta V = hf_{\text{rf}}/2e$.